



Chitosan/Carbon-Doped TiO₂ Composite for Adsorption of Two Anionic Dyes in Solution and Gaseous SO₂ Capture: Experimental Modeling and Optimization

Ahmed Saud Abdulhameed³ · Ali H. Jawad¹ · Muhammad Ridwan² · Tumirah Khadiran⁴ · Lee D. Wilson⁵ · Zaher Mundher Yaseen^{6,7,8}

Accepted: 5 July 2022 / Published online: 1 August 2022

© The Author(s), under exclusive licence to Springer Science+Business Media, LLC, part of Springer Nature 2022

Abstract

In this work, a chitosan (CHI) biopolymer was developed by loading different wt% of carbon-doped TiO₂ (C-TiO₂) with CHI to attain an efficient adsorbent of chitosan/carbon-doped TiO₂ (CHI/C-TiO₂). The fabricated materials were deployed for the removal of organic pollutants (methyl orange, MO; and reactive orange 16, RO16) and sulfur dioxide capture. The synthesized composites were characterized by BET, FTIR, XRD, TEM, SEM-EDX, pH_{pzc}, and pH-potentiometric titrations. Statistical modeling represented by the Box–Behnken design (BBD) was utilized for optimization of the impacts of the various parameters; A: C-TiO₂ particles loading (0–50%), B: dose (0.04–0.15 g), C: pH (4–10), and D: temperature (30–50 °C) on the adsorption of MO and RO16 dyes. The adsorption isotherms were obtained at equilibrium and under dynamic conditions, where the best fit to the isotherm results was shown by the Langmuir model and pseudo-first-order kinetic model, respectively. The maximum adsorption capacities of CHI/C-TiO₂-50 (containing 50% of C-TiO₂) was estimated at 196.6 mg/g and 270.5 mg/g for MO and RO16 dyes, respectively. This work revealed that the designed biomaterial (CHI/C-TiO₂-50) could be realized as an effective adsorbent for environmental remediation that includes decontamination of wastewater and SO₂ gas capture.

Keywords Adsorption · Box–Behnken design · Chitosan · Carbon-doped TiO₂ · Optimization

Introduction

Air and water pollution is one of the fundamental problems that pose a great threat to the ecosystem and human health. In recent years, industrial development has undergone

tremendous growth in various parts of the world, and consequently, increased water and air pollution can occur due to release of effluents containing chemicals into water bodies and release of toxic gases released into the atmosphere [1]. Organic dyes are one of the chemicals that are widely used

✉ Ali H. Jawad
ali288@uitm.edu.my; ahjm72@gmail.com

¹ Faculty of Applied Sciences, Universiti Teknologi MARA, 40450 Shah Alam, Selangor, Malaysia

² Department of Chemistry, Faculty of Mathematics and Natural Sciences, Universitas Indonesia, Depok 16424, Indonesia

³ Department of Medical Instrumentation Engineering, Al-Mansour University College, Baghdad, Iraq

⁴ Forest Products Division, Forest Research Institute Malaysia (FRIM), 52109 Kepong, Selangor, Malaysia

⁵ Department of Chemistry, University of Saskatchewan, 110 Science Place, Thorvaldson Building, Saskatoon, SK S7N 5C9, Canada

⁶ Department of Earth Sciences and Environment, Faculty of Science and Technology, Universiti Kebangsaan Malaysia, 43600 Bangi, Selangor, Malaysia

⁷ Adjunct Research Fellow, USQ's Advanced Data Analytics Research Group, School of Mathematics Physics and Computing, University of Southern Queensland, Toowoomba, QLD 4350, Australia

⁸ New Era and Development in Civil Engineering Research Group, Scientific Research Center, Al-Ayen University, Thi-Qar 64001, Iraq

in many industries such as textiles, pharmaceuticals, plastics, cosmetics, paper, and leather [2]. The release of these dyes into freshwater environments causes many problems for biota, such as reducing the effectiveness of photosynthesis, in addition to human health problems [3]. Methyl orange (MO) and reactive orange 16 (RO16) are among the azo dyes that are typical of anionic model organic pollutants [4, 5]. These dyes are non-degradable which makes them a great danger to aquatic environments, including their health hazards [6].

On the other hand, sulfur dioxide (SO_2) is considered one of the most harmful gases, which is produced from several industries such as the combustion of fossil fuels (e.g., coal, gas, and oil) in the power plants, and the smelting of mineral ores [7]. This gas causes several environmental phenomena such as photochemical smog, acid rain, and haze [8]. These phenomena can negatively affect climatic systems (e.g., the atmosphere, rivers, snow cover, and sea ice), plant communities, human health, and animal growth [8, 9]. In light of the foregoing, the treatment of wastewater containing organic pollutants and the removal of toxic gases before release into the environment is an urgent matter to preserve the ecosystem and human health. Several methods have been reported in the treatment of dyeing wastewater including adsorption [10], nanofiltration [11], photocatalytic degradation [12], and electrocoagulation [13], while in air pollution with SO_2 gas, the common methods applied for capturing SO_2 employ liquid alkaline solutions (e.g., $\text{Ca}(\text{OH})_2$, and $\text{Mg}(\text{OH})_2$), and adsorbent materials (e.g., activated carbon) [7]. In general, adsorption technology is a preferred method for pollutant removal from water and air. Adsorption is characterized by unique and favourable features (e.g., simplicity of design, low investment cost, lack of secondary pollution, removal efficiency, and regeneration ability) that position it at the forefront of methods applied to air and water pollution control [9, 14]. Activated carbon (AC) is one of the most popular adsorbents in the field of adsorption of air and water pollutants due to its amazing properties such as porosity, high adsorption capacity, high surface area, and thermal stability [15, 16]. Despite these impressive properties of AC, it is economically expensive to produce. For this reason, research efforts have shifted to low-cost, renewable, and environmentally friendly adsorbents.

Chitosan (CHI) is one of the most environmentally friendly, renewable, and efficient adsorbents employed in adsorption technology [17]. In acidic media, CHI is a natural cationic polysaccharide that consists of glucosamine units [18]. CHI has several unique advantages over other common adsorbents, such as its ease of modification, biodegradability, super absorbency, hydrophilicity, and nontoxicity [19]. The chemical structure of CHI is characterized by abundant amino and hydroxyl groups, which are likely to be active adsorption sites for the removal of acid gases such as SO_2

and acid dyes [20, 21]. Despite the foregoing, some of the properties of CHI require further development such as the effective surface area, chemical stability, and mechanical strength. Several strategies have been employed in developing the CHI properties such as composite formation with inorganic materials [22], grafting with organic groups [23], and crosslinking [24]. The development of CHI by composite formation with inorganic materials has attracted much attention due to its extraordinary properties like improved surface area, absorption capacity, chemical stability, and mechanical strength [22].

Carbon-doped TiO_2 (known as Kronos) is one of the most promising materials that can be employed in modifying the properties of CHI due to its distinctive characteristics such as its surface area, chemical stability, mechanical strength, photo activity, and adsorption efficiency of inorganic/organic contaminants [25, 26]. Many studies have reported on the development of CHI by TiO_2 and its utilization in various applications such as wastewater treatment [27], biosensor [28], and antimicrobial [29], but with carbon-doped TiO_2 (C- TiO_2), no studies were reported thus far. Furthermore, the CHI-based composites for capturing hazardous gases were recently explored, for example, CHI grafted Leca biocomposite for the capture of carbon dioxide (CO_2) [30], adsorption of formaldehyde gas by CHI crosslinked with MOF-199@ aminated graphene oxide aerogel [31], CHI extracted from shrimp shells loaded with Cd ions for the capture of hydrogen sulfide (H_2S) [32], CHI aerogel for the removal of ammonia (NH_3) gas [33], and ferrocene-CHI for sorption of carbon monoxide (CO) gas [34].

Herein, this study aims to develop a CHI biopolymer by loading different wt% of C-doped TiO_2 onto CHI to attain an efficient adsorbent, referred to as CHI/C-doped TiO_2 (CHI/C- TiO_2). The synthesized composites were fully characterized by BET, FTIR, XRD, TEM, SEM-EDX, pH_{pzc} , and pH-potentiometric titrations. The fabricated materials were applied for the removal of organic pollutants (MO and RO16) and SO_2 capture. Statistical modeling represented by Box-Behnken design (BBD) was utilized for optimization of the impacts of the C- TiO_2 particles loading, dose, pH, and temperature on the adsorption of MO and RO16 dyes. In addition, several kinetic and isothermal models have been utilized to investigate the adsorption properties and mechanism of the CHI/C- TiO_2 composite.

Materials and Methods

Materials

Chitosan (CHI, deacetylation $\geq 75\%$), and Carbon-doped TiO_2 (C- TiO_2 , Kronos) were supplied by Sigma-Aldrich. The organic dyes including methyl orange

(MO; $C_{14}H_{14}N_3NaO_3S$; MW: 327.32; $\lambda_{max} = 464$ nm), and reactive orange 16 (RO16; $C_{20}H_{17}N_3Na_2O_{11}S_3$; MW: 617.54 g/mol; $\lambda_{max} = 493$ nm) were obtained from ACROS, Organics. The chemicals including acetic acid (CH_3COOH), sodium chloride (NaCl), sodium hydroxide (NaOH), and hydrochloric acid (HCl) were obtained from R&M Chemicals.

Synthesis of CHI/C-TiO₂

The synthesis of CHI/C-TiO₂ was based on the approach described in previous work [35]. Initially, 1 g of CHI flakes was poured into 60 ml of CH_3COOH acid solution (5% v/v) and stirred at 500 rpm on a magnetic stirrer for 24 h at 25 °C to dissolve the CHI flakes. Then, the CHI solution was added drop-wise into 1000 ml NaOH (2 M) solution to obtain CHI beads. The resulting CHI hydrogel beads were washed with distilled water until the pH became neutral. For comparison, CHI/C-TiO₂ composites were fabricated by loading different wt. % of C-TiO₂ with CHI before adding to the solution of CH_3COOH , i.e. 25:75 wt% (C-TiO₂:CHI), which was termed as CHI/C-TiO₂-25 and 50:50. wt% (C-TiO₂:CHI), which was termed as CHI/C-TiO₂-50. Finally, the fabricated composites were crushed and then sieved to particle size (250 μ m) for the dye removal tests, along with SO₂ capture.

Characterization

The textile properties (e.g., specific surface area, and average pore width) of the CHI/C-TiO₂-50 were obtained through Brunauer–Emmett–Teller (BET) method (Micromeritics ASAP 2060). The morphological characteristics of CHI/C-TiO₂-50 before and after adsorption of MO and RO16 dyes were achieved by recording scanning electron microscope (SEM, Zeiss Supra 40 VP) images. The energy dispersive X-Ray analysis (EDX) was performed to the chemical qualitative analysis of the CHI/C-TiO₂-50 before and after adsorption of MO and RO16 dyes. X-ray powder diffraction spectra (XRD, X'Pert PRO, PANalytical) were used to evaluate the phase determination of the CHI/C-TiO₂-50 composite. Fourier Transform Infrared (FTIR) spectra (Perkin-Elmer, Spectrum RX I) was used to determine the surface chemical characteristics of the CHI/C-TiO₂-50 composite before and after MO and RO16 dyes adsorption. The free amino (-NH₂) groups in the CHI/C-TiO₂-50 was computed by pH-potentiometric titrations [36]. Zero-point of charge (pH_{pzc}) analysis was employed to determine the surface charge of the CHI/C-TiO₂-50 [37].

Experimental modeling

BBD was used in this research work as an efficient and reliable statistical method to provide MO removal (%) and RO16

removal (%) as responses based on several independent factors that affect the adsorption properties: C-TiO₂ loading, pH, adsorbent dosage, and temperature. The statistical analysis and numerical demonstration of the experimental results related to MO and RO16 removal were acquired through the software program of Design-Expert (Stat-Ease, version 13). Table 1 shows the parameters evaluated inside the BBD model, along with their levels and symbols. A polynomial equation (Eq. 1) was applied to correlate the experimental results and estimate the MO removal (%) and RO16 removal (%).

$$Y = \beta_0 + \sum \beta_i X_i + \sum \beta_{ii} X_i^2 + \sum \sum \beta_{ij} X_i X_j \quad (1)$$

where Y , and (X_i and X_j) symbol the forecasted response (MO removal (%) or RO16 removal (%)); and the evaluated factors. β_0 and β_i , denote the regression coefficients of intercept, and the linear; whereas, β_{ii} and β_{ij} signify quadratic and interaction effects. The BBD model produced 29 runs to examine the influence of the following factors: A: C-TiO₂ loading (0–50%), B: adsorbent dose (0.04–0.15 g), C: pH (4–10), and D: temperature (30–50 °C) on MO and RO16 dyes adsorption process. The actual values of responses (MO and RO16 removal) along with their experimental conditions are recorded in Table 2. In 250 ml flasks that contain 100 ml of the dye solution, a constant quantity of the adsorbent was added. Then, these sealed flasks were transferred into a shaker water bath (WNB7-45, Memmert) at a speed of up to 90 strokes/min. The next step after the adsorption process was to remove the adsorbents from solutions with a syringe filter (0.45 μ m). Then, the residual concentrations of MO and RO16 in solutions was estimated using spectrophotometry with a UV-Vis spectrometer (HACH DR 2800) at λ_{max} 464 nm and 493 nm, respectively. The removal efficiency (R , %) of MO and RO16 dyes were calculated using Eq. 2 shown below.

$$R\% = \frac{(C_o - C_e)}{C_o} \times 100 \quad (2)$$

where C_o (mg/L) and C_e (mg/L) represent the dye concentrations (MO or RO16) before and after the adsorption process, respectively.

Table 1 Coded and actual variables and their levels in BBD

Codes	Variables	Level 1 (-1)	Level 2 (0)	Level 3 (+1)
A	C-TiO ₂ loading (%)	0	25	50
B	Dose (g)	0.04	0.095	0.15
C	pH	4	7	10
D	Temperature (°C)	30	40	50

Table 2 The 4-variables BBD matrix and experimental data for MO removal and RO16 removal

Run	A: C-TiO ₂ loading (%)	B: Dose (g)	C: pH	D: Temp. (°C)	MO removal (%)	RO16 removal (%)
1	0	0.04	7	40	4.1	8.4
2	50	0.04	7	40	18.8	23.7
3	0	0.15	7	40	12.7	15.1
4	50	0.15	7	40	72.2	77.7
5	25	0.095	4	30	40.8	52.2
6	25	0.095	10	30	15.9	23.5
7	25	0.095	4	50	50.5	58.4
8	25	0.095	10	50	9.7	14.7
9	0	0.095	7	30	6.3	10.3
10	50	0.095	7	30	66.6	81.1
11	0	0.095	7	50	9.3	18.8
12	50	0.095	7	50	75.4	85.8
13	25	0.04	4	40	18	23.3
14	25	0.15	4	40	58.5	74.2
15	25	0.04	10	40	6.5	12.8
16	25	0.15	10	40	10.2	13.2
17	0	0.095	4	40	7.2	15.9
18	50	0.095	4	40	81.6	90.4
19	0	0.095	10	40	2.5	3.4
20	50	0.095	10	40	30.3	34.4
21	25	0.04	7	30	8.2	12.9
22	25	0.15	7	30	20.9	24
23	25	0.04	7	50	8.4	14.5
24	25	0.15	7	50	35.9	44.4
25	25	0.095	7	40	18.5	23.4
26	25	0.095	7	40	17.9	24.2
27	25	0.095	7	40	18.2	23.8
28	25	0.095	7	40	18.3	24.5
29	25	0.095	7	40	17.5	23.8

Adsorption study of MO and RO16 dyes on CHI/C-TiO₂-50

Determining the adsorption ability of CHI/C-TiO₂-50 toward MO and RO16 dyes was accomplished by use of batch experiments. As determined in Table 2, the maximum removal of MO (81.6%) and RO16 (90.4%) dyes was accomplished in run eighteen under the following conditions: C-TiO₂ loading = 50%, dosage = 0.095 g (adjusted to 0.1 g in adsorption tests), pH 4, and temperature = 40 °C. In this way, batch tests were carried out to study the uptake the MO and RO16 dyes at these previously mentioned ideal conditions over a range of initial concentrations (20–200 mg/l). The calculation of the adsorption capacity (q_e , mg/g), of MO and RO16 dyes on the surface of the CHI/C-TiO₂-50 at equilibrium employed Eq. 3.

$$q_e = \frac{(C_o - C_e)V}{W} \quad (3)$$

where W (g) and V (L) are the amount of CHI/C-TiO₂-50 and the volume of the dye solution (MO and RO16), respectively.

SO₂ adsorption tests

The SO₂ adsorption tests were carried out by Ultramat 23 Gas Analyzer integrated with computer dynamic simulation to adjust the gas flow rate of SO₂ for the tests. 1 g of the synthesized adsorbent was placed in the reaction vessel and the temperature was maintained at 87 °C. Before SO₂ capture, N₂ (99.99%) was passed through the prepared adsorbent to exclude any undesired compounds. After that, a stream of SO₂ (1000 ppm) gas was fed to the column containing

adsorbent meanwhile keeping on the feed flow at 500 ml/min. Equation 4 was utilized to calculate the breakthrough adsorption capacity (S , mmol/g) of SO_2 gas.

$$S = \frac{10^{-6} q \int_0^{t_m} (C_0 - C_i) dt}{22.4G} \quad (4)$$

where q , t_m , and G signify the gas flow rate (ml/min), is the breakthrough time (min), and the amount of the adsorbent (g). C_0 and C_i represent the initial concentration (ppm), and the outlet concentration (ppm) of SO_2 gas.

Results and discussion

Characterization of the CHI/C-TiO₂-50

Table 3 lists the physicochemical properties of the CHI/C-TiO₂, specifically the amine content (%) and surface area characteristics. pH-potentiometric titration is a vital method used to estimate the proportion of primary amino groups (-NH₂) existing in the backbone of the CHI/C-TiO₂-50, which symbolizes adsorptive sites for anionic dyes such as MO and RO16 dyes. The -NH₂ content in CHI/C-TiO₂-50 determined by potentiometric titration reached 38.41%. This finding suggests that the CHI/C-TiO₂-50 still has plenty of -NH₂ to bind with MO and RO16 dyes. The results of the BET analysis showed that the surface area of the CHI/C-TiO₂-50 composite is significantly higher than the cross-linked CHI composites containing 50% of TiO₂ nanoparticles. For example, cross-linked CHI-glyoxal/TiO₂ (17.74 m²/g) [38] and cross-linked CHI-tripolyphosphate/TiO₂ (2.75 m²/g) [35] indicate that C-TiO₂ possesses a high surface area that plays a significant role in improving the surface properties of CHI/C-TiO₂-50 through supporting onto the CHI biopolymer matrix. As per IUPAC, CHI/C-TiO₂-50 is a mesoporous material due to its average pore diameter of 7.31 nm.

The X-ray diffraction (XRD) profile of the CHI/C-TiO₂-50 composite is illustrated in Fig. 1. The broad peak located at 20.3° in Fig. 1 relates to the semi-crystalline nature of CHI biopolymer [39]. In Fig. 1, several peaks at 2θ of

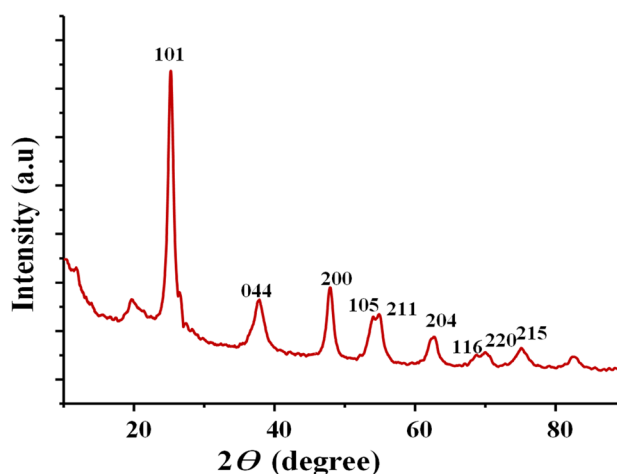


Fig. 1 XRD pattern of CHI/C-TiO₂-50

25.28°, 37.8°, 48.05°, 53.89°, 55.1°, 62.6°, 68.7°, 70.3° and 75.01° correspond to the [101], [004], [200], [105], [211], [204], [116], [220], and [215] crystalline phases of C-TiO₂, respectively with the Miller indices (JCPDS file No. 00-021-1272) [40].

TEM analysis was performed to accurately determine the particle size of C-TiO₂. The TEM images of C-TiO₂ particles at several wavelengths (500 nm, 200 nm, 100 nm, and 50 nm) are illustrated in Fig. 2a–d, respectively. According to the TEM results in Fig. 2, the size of C-TiO₂ particles is 8.60 nm (Fig. 2d). These results concur with the results of the BET analysis, which support that the surface area of the CHI/C-TiO₂-50 was 89.34 m²/g. The presence of nano-sized particles (C-TiO₂) in the formula designed (CHI/C-TiO₂-50) for adsorption of anionic dyes and SO₂ gas impart a high adsorption efficiency to remove organic and inorganic pollutants.

The surface functional groups of the CHI/C-TiO₂-50, and CHI/C-TiO₂-50 after MO and RO16 dyes adsorption were determined by FTIR analysis. The FTIR spectra of CHI/C-TiO₂-50, and CHI/C-TiO₂-50 after the adsorption of MO and RO16 dyes are shown in Fig. 3a–c. The characterized bands of CHI/C-TiO₂-50 composite (Fig. 3a) at 3698 cm⁻¹, 3500–3650 cm⁻¹, 2270 cm⁻¹, 1660 cm⁻¹, 1450 cm⁻¹, 1380 cm⁻¹, 1075 cm⁻¹, 770 cm⁻¹, and 540 cm⁻¹ are attributed to the hydroxyl groups of TiO₂, -OH and -NH₂ stretching, stretching of C≡C, N-H bending vibration, deformations of C-O-H, C-N stretching, C-O-C stretching, stretching vibration of Ti-O-Ti and Ti-O bond, respectively [41, 42]. The FTIR spectra of the CHI/C-TiO₂-50 composite after MO (Fig. 3b) and RO16 (Fig. 3c) adsorption showed a remarkable change in the bands of -NH₂ and -OH groups, which is notably shifted, and broadened, confirming that the -OH and NH₂ groups participate in the MO and RO16 adsorption process. Besides, the peak at 1500 cm⁻¹ can be

Table 3 The physicochemical properties of the CHI/C-TiO₂-50

Property	Value
-NH ₂ content (%)	38.41
BET surface area (m ² /g)	89.34
Langmuir surface area (m ² /g)	127.6
Total pore volume (cm ³ /g)	0.1346
V _m (cm ³ /g)	0.00328
Mean pore diameter (nm)	7.31

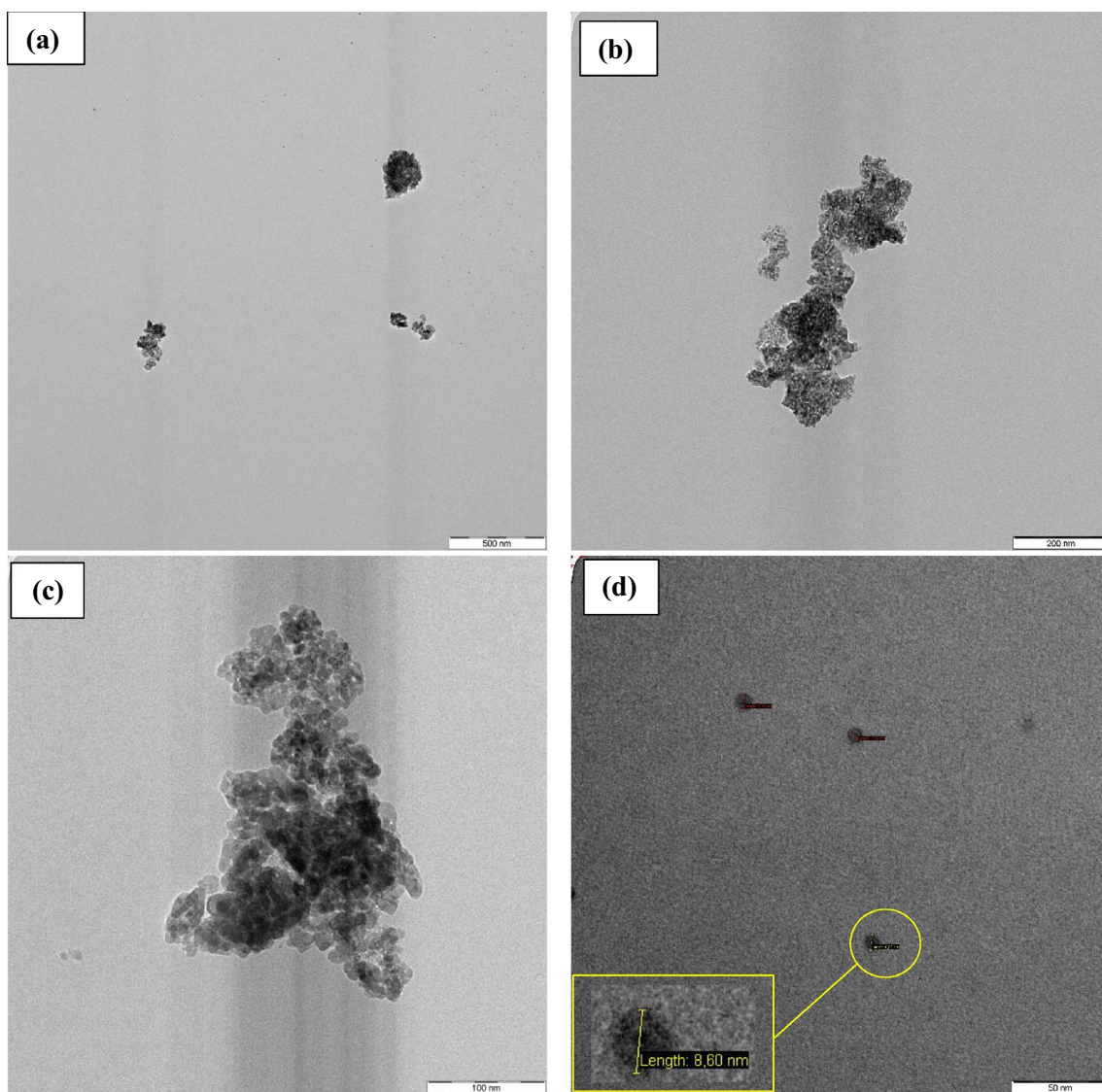


Fig. 2 The TEM images of C-TiO₂ particles at variable magnification namely **a** 500 nm, **b** 200 nm, **c** 100 nm, and **d** 50 nm

attributed to the aromatic rings (C=C) of the MO and RO16 dyes further confirm the loading or adsorption of MO and RO16 dyes onto the CHI/C-TiO₂-50 surface.

Exploration of the surface morphology of the CHI/C-TiO₂-50 before and after adsorption of MO and RO16 dyes as well as estimates of its chemical composition was achieved by SEM-EDX. Figure 4a–c provides SEM-EDX images of (a) CHI/C-TiO₂-50, and CHI/C-TiO₂-50 following adsorption of (b) MO and (c) RO16 dyes. As seen in Fig. 4a, the surface features for the 50% C-TiO₂ particles loaded onto CHI reveal that the CHI/C-TiO₂-50 had a granular surface containing tiny pores, which illustrates the embedding of C-TiO₂ particles onto the polymer matrix of CHI. The EDX spectrum of the CHI/C-TiO₂-50 reveals the presence of Ti, O, C, and N. The appearance of a Ti signature in the EDX spectrum is further evidence that

the C-TiO₂ particles were effectively incorporated onto the CHI matrix. The CHI/C-TiO₂-50 surface was altered into a smooth, packed, and uniform surface after adsorption of MO (Fig. 4b) and RO16 (Fig. 4c), consistent with the uniform dye surface coverage. This result was confirmed by EDX, which showed that the content of C (%) was increased because of loading the dye (MO or RO16) molecules.

Model validation

A statistical analysis of variance (ANOVA), including the statistical evaluation of the significant impacts of the factors and their interactions related to the MO and RO16 dyes removal was carried out. The ANOVA findings for the removal of the MO and RO16 dyes are listed in Table 4. The MO and RO16 removal models have F-values of 23.63

and 18.12, respectively, implying that the models are critical [43]. The correlation coefficients (R^2) of 0.96 (MO removal) and 0.95 (RO16 removal) indicate that the models are well fitted and that there is a favourable agreement between theoretical and actual removal values [44]. Statistically, the BBD model terms have statistical significance when the p -value ≤ 0.05 . Accordingly, A, B, C, AB, AC, BC, A^2 , and D^2 are critical terms in the removal process of the MO and RO16 dyes. Along these lines, the linkage between MO and RO16 removal with the examined variables was empirically fitted by the quadratic polynomial formula, as expressed in Eqs. 5 and 6, respectively.

$$\begin{aligned} \text{MO removal (\%)} = & +18.08 + 25.23A + 12.20B - 15.13C + 11.20AB \\ & - 11.65AC - 9.20BC + 11.40A^2 + 6.51D^2 \end{aligned} \quad (5)$$

$$\begin{aligned} \text{RO16 removal (\%)} = & +23.94 + 26.77A + 12.75B - 17.70C + 11.82AB \\ & - 10.88AC - 12.63BC + 11.44A^2 + 8.39D^2 \end{aligned} \quad (6)$$

Analysis of the diagrams inclusive of real versus predicted, where the normal probability of the residuals might be utilized to successfully verify the experimental findings of dye removal for MO and RO16. The real vs. expected graphs of MO and RO16 removal values are shown in Fig. 5a, b, where the real points were largely near the predicted points, demonstrating that the BBD model can optimize the adsorption process for these dyes. The normal probability charts of the MO and RO16 removal dyes are depicted in Fig. 5c, d. As seen from Fig. 5c, d, the typical distribution of dots around the straight-line denote the independence of the residuals [41].

Adsorption optimization of MO and RO16 dyes

3D response surfaces plots are as one of the main graphical representations that provide an understanding of the nature of the fundamental interactions among the two investigated variables and their impacts on the responses denoted by the MO removal and RO16 removal. The cumulative impacts of C–TiO₂ loading and dosage (termed as AB interaction) on the MO and RO16 removal were meaningful. Figure 6a, b displays the 3D surface plot of the cumulative impacts of AB interaction on the MO and RO16 removal at the accompanying fixed circumstances: pH (7) and temperature (40 °C). The findings shown in Fig. 6a, b found that increasing the adsorbent dosage and C–TiO₂ loading enhances the removal of MO and RO16 dyes. Such findings are related to the excessive surface area coming from C–TiO₂ particles and the adequate quantity of reactive sites available on the CHI/C–TiO₂ surface, which are attracted with MO and RO16 molecules to obtain the adsorption process.

The cumulative impacts of C–TiO₂ loading vs. pH (termed as AC interaction) and dose vs. pH (termed as BC interaction) on the MO and RO16 removal were meaningful. Figure 7a–d displays the 3D surface plot of the cumulative impacts of AC and BC interactions on the MO and RO16 removal at the accompanying fixed conditions: dose (0.095 g) and temperature (40 °C) for AC interaction; and C–TiO₂ loading (25%) and temperature (40 °C) for BC interaction. As demonstrated in Fig. 7a–d, the MO and RO16 (%) improved simultaneously with a pH drop from 10 to 4. As shown in Fig. 7e, pH_{pzc} of the CHI/C–TiO₂-50 equals 7.0. This observation indicates that the CHI/C–TiO₂ surface acquires negative charges at pH values larger than pH_{pzc} . As a result of the rise in H^+ concentration in the solution, the CHI/C–TiO₂ surface becomes positively charged at an acidic medium. Therefore, the electrostatic attractions between the sulfonate ($-SO_3^-$) groups belonging to the MO and RO16

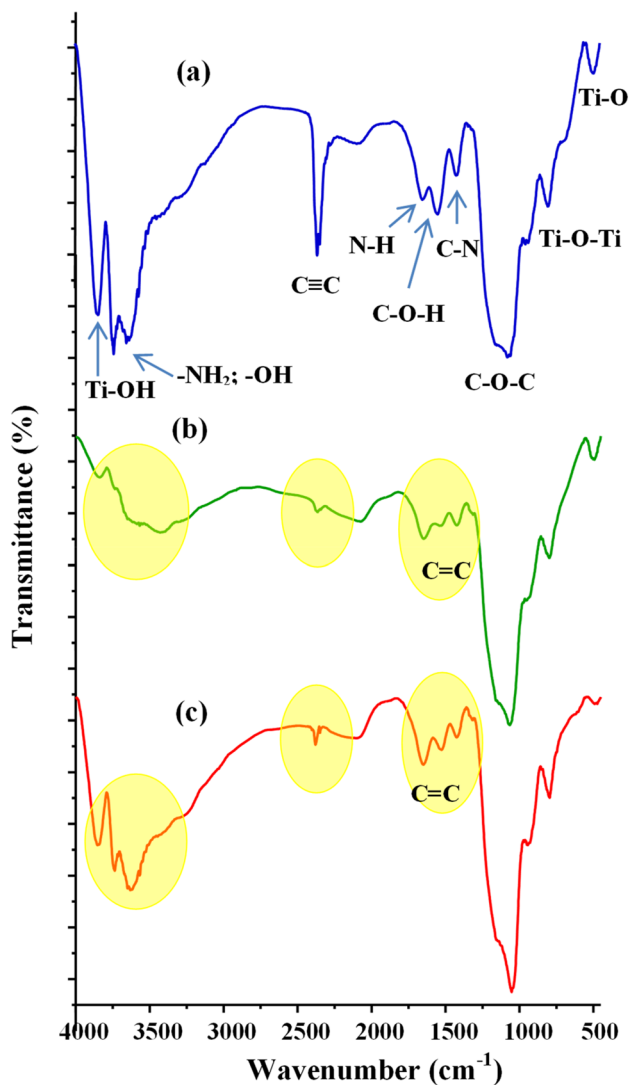


Fig. 3 FTIR spectra of **a** CHI/C–TiO₂-50, and CHI/C–TiO₂-50 after adsorption of **b** MO and **c** RO16 dyes

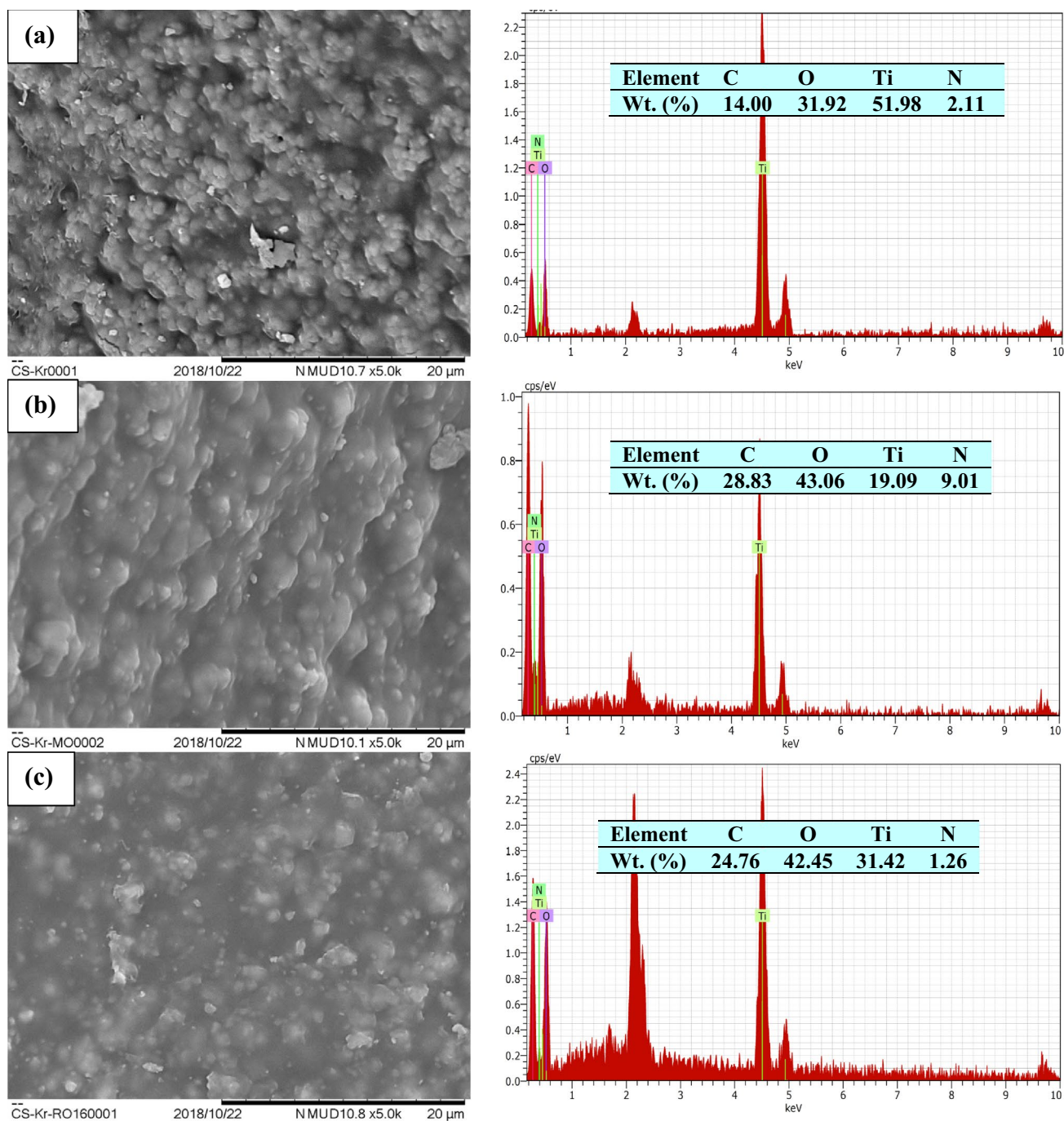
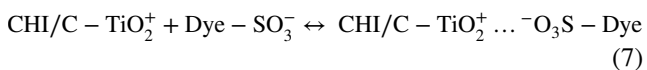


Fig. 4 SEM–EDX images of **a** CHI/C–TiO₂-50, and CHI/C–TiO₂-50 after adsorption of **b** MO and **c** RO16 dyes

dyes and cationic groups of CHI/C–TiO₂-50, as shown in Eq. 7.



where the Dye – SO₃[–] indicates either the MO or the RO16 dye species.

Adsorption study

An investigation on the effect of initial concentration on the adsorption behaviour of MO and RO16 dyes by the CHI/C–TiO₂-50 composite was performed at several dye adsorbate concentrations (20–200 mg/l); whereas, the mass of the adsorbent (0.095 g), volume of the dye

Table 4 Analysis of variance (ANOVA) for MO removal and RO16 removal

MO removal						RO16 removal				
Source	Sum of Squares	df	Mean Square	F-value	p-value	Sum of Squares	df	Mean Square	F-value	p-value
Model	14,980.28	14	1070.02	23.63	<0.0001	17,714.65	14	1265.33	18.12	<0.0001
A	7640.65	1	7640.65	168.70	<0.0001	8597.45	1	8597.45	123.14	<0.0001
B	1786.08	1	1786.08	39.44	<0.0001	1950.75	1	1950.75	27.94	0.0001
C	2745.19	1	2745.19	60.61	<0.0001	3759.48	1	3759.48	53.85	<0.0001
D	77.52	1	77.52	1.71	0.2119	88.56	1	88.56	1.27	0.2790
AB	501.76	1	501.76	11.08	0.0050	559.32	1	559.32	8.01	0.0134
AC	542.89	1	542.89	11.99	0.0038	473.06	1	473.06	6.78	0.0209
AD	8.41	1	8.41	0.1857	0.6731	3.61	1	3.61	0.0517	0.8234
BC	338.56	1	338.56	7.48	0.0161	637.56	1	637.56	9.13	0.0091
BD	54.76	1	54.76	1.21	0.2901	88.36	1	88.36	1.27	0.2795
CD	63.20	1	63.20	1.40	0.2572	56.25	1	56.25	0.8057	0.3846
A ²	842.61	1	842.61	18.60	0.0007	849.28	1	849.28	12.16	0.0036
B ²	46.50	1	46.50	1.03	0.3281	86.77	1	86.77	1.24	0.2837
C ²	130.48	1	130.48	2.88	0.1117	186.88	1	186.88	2.68	0.1241
D ²	274.90	1	274.90	6.07	0.0273	456.87	1	456.87	6.54	0.0228
Residual	634.08	14	45.29			977.46	14	69.82		
Cor total	15,614.37	28				18,692.11	28			

solution (100 ml), pH (4), and temperature (40 °C) were held constant. The adsorption property of CHI/C–TiO₂ towards MO and RO16 dyes as a function of contact time are shown in Fig. 8a, b. In Fig. 8a, b, the adsorption capacity of CHI/C–TiO₂-50 was found to increase from 17.9 to 148.4 mg/g for MO and from 20.4 to 193.7 mg/g for RO16, across a range of dye concentration (20 to 200 mg/l). The higher concentration range for MO and RO16 provides an important driving force that contributes to the transport of MO and RO16 molecules to the available active sites on the CHI/C–TiO₂-50 surface [45].

SO₂ capture

The removal of SO₂ over CHI biopolymer in the presence and absence of variable C–TiO₂ loadings was investigated. Figure 9 displays the breakthrough curves of SO₂ capture over CHI biopolymer, CHI/C–TiO₂-25, and CHI/C–TiO₂-50. According to the breaking curves exhibited in Fig. 9, the saturation time of CHI biopolymer, CHI/C–TiO₂-25, and CHI/C–TiO₂-50 was 11 min, 30 min, and 35 min, respectively. These results concur with the values of SO₂ adsorption capacity listed in parentheses as follows: CHI/C–TiO₂-25 (0.6140 mmol/g), CHI/C–TiO₂-50 (0.7622 mmol/g), and CHI biopolymer (0.1342 mmol/g). Therefore, the SO₂ adsorption data revealed that SO₂ capture by the CHI/C–TiO₂-25 and CHI/C–TiO₂-50 biomaterials was significantly improved compared to the CHI biopolymer. The improvement in adsorption performance of CHI biopolymer (without C–TiO₂ particles) upon loading with C–TiO₂

loading (especially 50%) for CHI/C–TiO₂-50 (89.34 m²/g) can be attributed to the greater surface area effects of the C–TiO₂ particles. In addition to the above, and from a chemical point of view, CHI/C–TiO₂-50 possesses active adsorption sites such as Ti–O, C–O, –OH, and –NH₂, which can participate in the binding of SO₂ molecules [8, 20]. Fundamentally, the SO₂ capture occurred at a high temperature of 360 K, which signifies that the surface sulfate-like species (SO₄²⁻) was formed from the SO₂ capture process is activated by elevated temperature [46].

Kinetic study

In order to understand the adsorption behavior and determine the control mechanism responsible for the adsorption of MO and RO16 dyes on the surface of CHI/C–TiO₂-50, the experimental data were evaluated by common kinetics model equations, via the pseudo-first-order (PFO) [47] and pseudo-second-order (PSO) models [48]. The terms of the kinetics including PFO and PSO were extracted by the non-linear formulas listed in Eqs. 8 and 9, respectively.

$$q_t = q_e(1 - \exp^{-k_1 t}) \quad (8)$$

$$q_t = \frac{q_e^2 k_2 t}{1 + q_e k_2 t} \quad (9)$$

where q_e (mg/g) and q_t (mg/g) represent the adsorption capacities at equilibrium and time (t), respectively. k_1 (1/min) and k_2 (g/mg min) are the rate constants of the

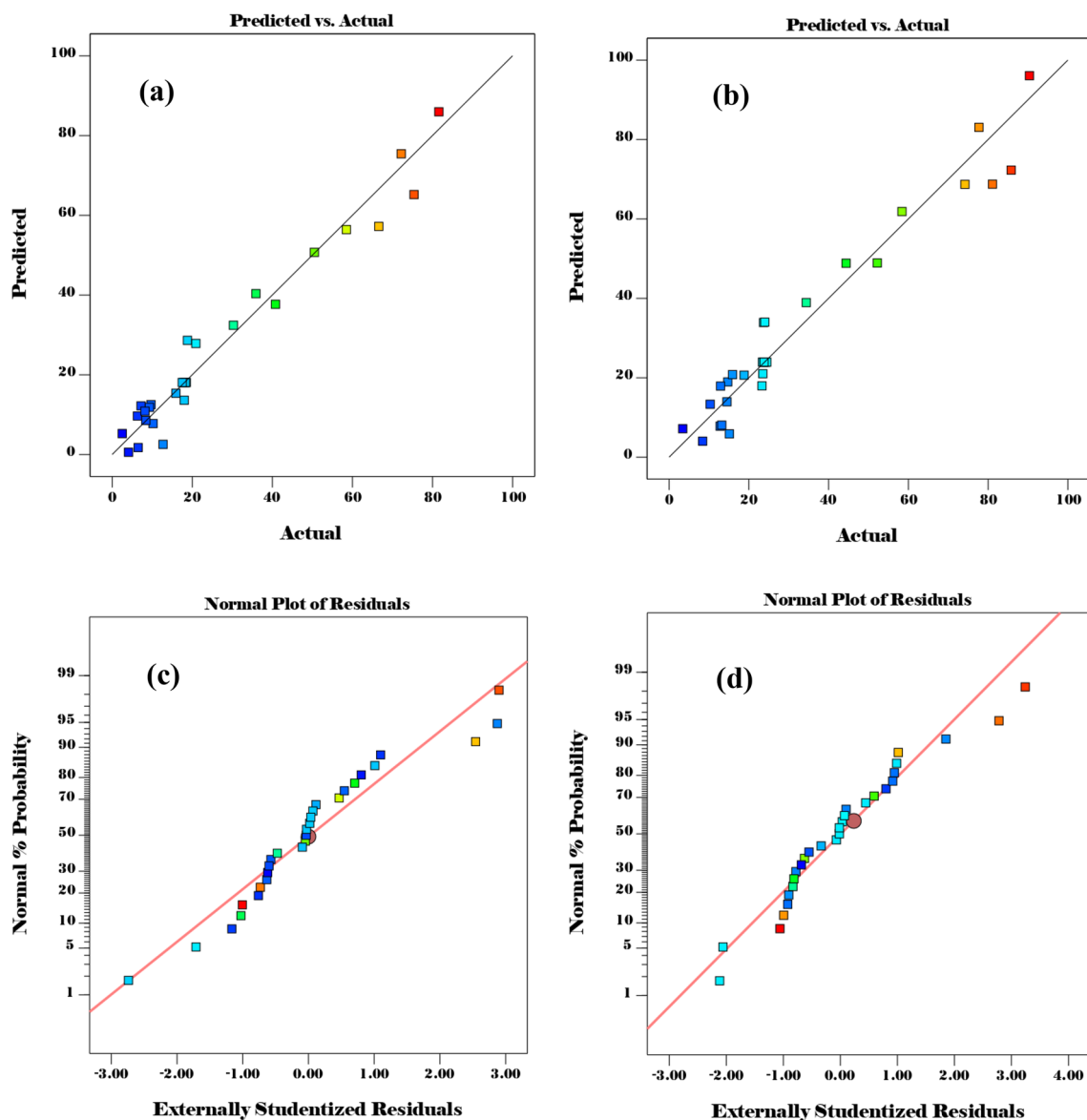


Fig. 5 Plots the relationship between the actual and predicted values of **a** MO and **b** RO16 removal; the normal probability of residuals for **c** MG and **d** RO16 removal

PFO and PSO kinetic models, respectively. The calculated kinetic parameters are recorded in Table 5, where it can be concluded that the adsorption process for both dyes are described by the PFO model over that of the PSO model. This trend is supported by the relatively high R^2 values of PFO compared to the R^2 values of PSO, in addition to the experimental q_e values, which are closer to the calculated q_e values of the PFO model, in comparison with the calculated q_e values of PSO. The results reported herein support that the adsorption of the MO and RO16 dyes on CHI/C-TiO₂-50 is physisorption that

involves electrostatic attractions [49]. The latter occurs between the cationic groups present on the surface of CHI/C-TiO₂-50 and the -SO₃⁻ groups of the MO and RO16 dyes, respectively.

Isotherm study

An account of the mode of interaction between CHI/C-TiO₂-50 and the MO and RO16 dye species can be obtained by analysis of the equilibrium isotherms. The adsorption capacity of CHI/C-TiO₂-50 for the uptake MO and RO16 dyes

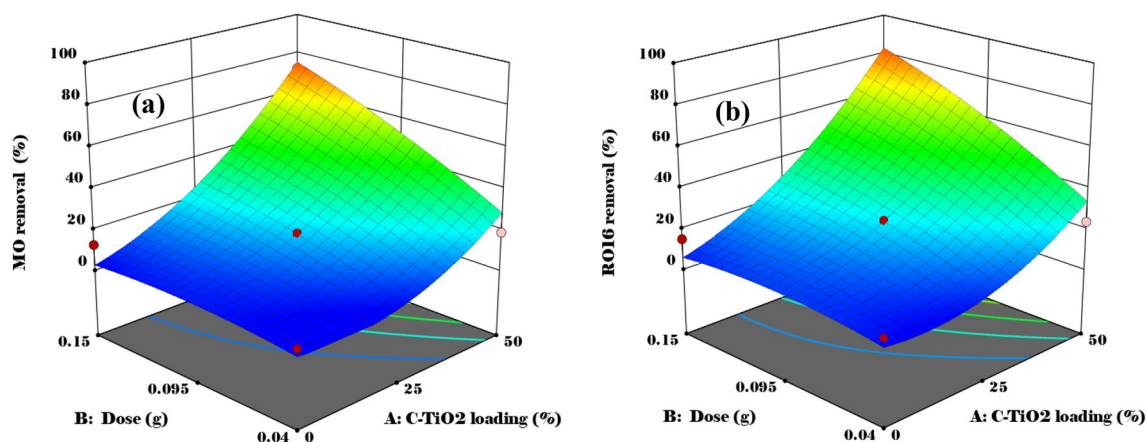


Fig. 6 3D surface plots of the cumulative impacts of AB interaction toward **a** MO and **b** RO16 removal

from the liquid phase was determined through the fitting of the experimental results to equilibrium isotherms like Langmuir, Freundlich, and Temkin [50–52]. The terms of the isotherms including Langmuir, Freundlich, and Temkin were extracted by the non-linear formulae listed in Eqs. 10–12, respectively.

$$q_e = \frac{q_{\max} K_a C_e}{1 + K_a C_e} \quad (10)$$

$$q_e = K_f C_e^{1/n} \quad (11)$$

$$q_e = \frac{RT}{b_T} \ln(K_T C_e) \quad (12)$$

K_a (L/mg), K_T (L/mg), and K_f (mg/g) (L/mg)^{1/n}, are the adsorption constants of Langmuir, Temken, and Freundlich isotherms. q_{\max} (mg/g) is the adsorption capacity of the CHI/C–TiO₂-50. n is the exponent term for the Freundlich model. b_T (J/mol) is a term related to the heat adsorption. T (K) and R (8.314 J/mol K) denote the temperature and universal gas constant, respectively. The curves acquired from adsorption isotherms for MO and RO16 dyes are exhibited in Fig. 10a, b while the calculated terms of the isotherms are given in Table 6. Depending on the R^2 values, it can be concluded that the adsorption of MO and RO16 dyes by CHI/C–TiO₂-50 fit better with the Langmuir isotherm model, based on the highest R^2 value compared to the other models. These findings signify the homogeneous character of the adsorbent surface for CHI/C–TiO₂-50 with the MO

and RO16 dyes [53]. The q_{\max} values for MO and RO16 dyes on CHI/C–TiO₂-50 were estimated as 196.6 mg/g and 270.5 mg/g at 40 °C, respectively. In order to get a better idea of the CHI/C–TiO₂-50's adsorption capacity, it was compared with the adsorption capabilities of other materials studied for the removal of such anionic dyes (MO and RO16), according to the values listed in Table 7. These results show that the CHI/C–TiO₂-50 poses a good ability to remove organic pollutants, specifically anionic dyes from polluted water.

Adsorption mechanism of MO and RO16 dyes

The surface of CHI/C–TiO₂ is characterized by an enormous amount of active groups such as hydroxyl (–OH), amino (–NH₂), and (Ti–OH), as per the FTIR spectrum, which is consistent with other studies [35, 38]. Because of the existence of such functional groups, the mechanism of MO and RO16 dye adsorption on the surface of CHI/C–TiO₂ was deduced, as seen in Fig. 11. One of the key pathways contributing to the adsorption of MO and RO16 dyes on the surface of CHI/C–TiO₂ is electrostatic forces that achieve by the attraction between the negative charge of the MO and RO16 dyes and the negatively charged groups of the CHI/C–TiO₂ surface as shown in Fig. 11. The interaction between the hydrogen on the CHI/C–TiO₂ surface and the nitrogen and oxygen atoms in the MO and RO16 dye structures is another probable interaction contributing to the adsorption of MO and RO16 dyes, which is called H-bonding. The π - π stacking is also

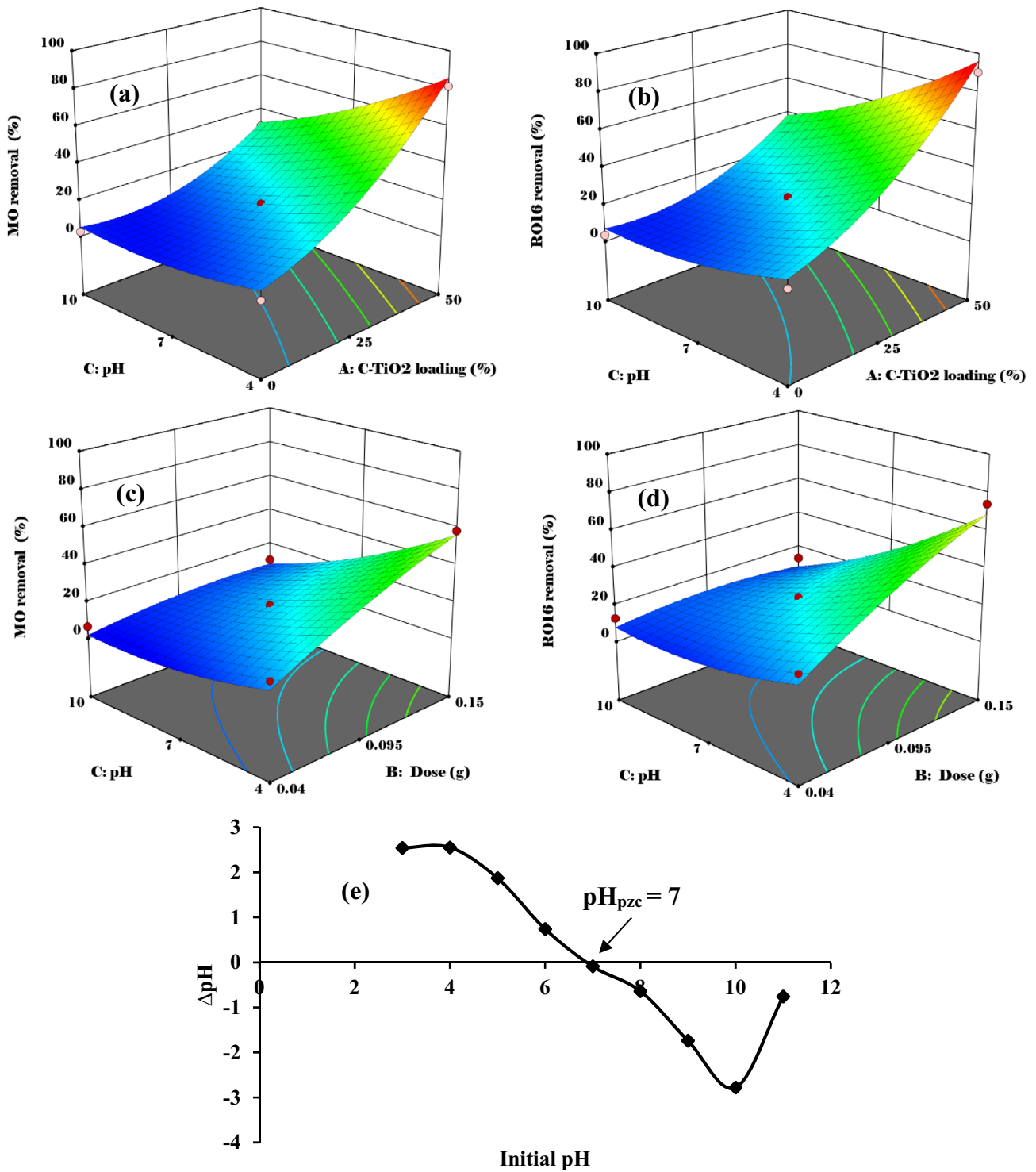


Fig. 7 3D surface plots of AC (a MO and b RO16) and BC (c MO and d RO16) interactions on the MO and RO16 removal; along with, e pH_{pzc} of CHI/C-TiO₂-50

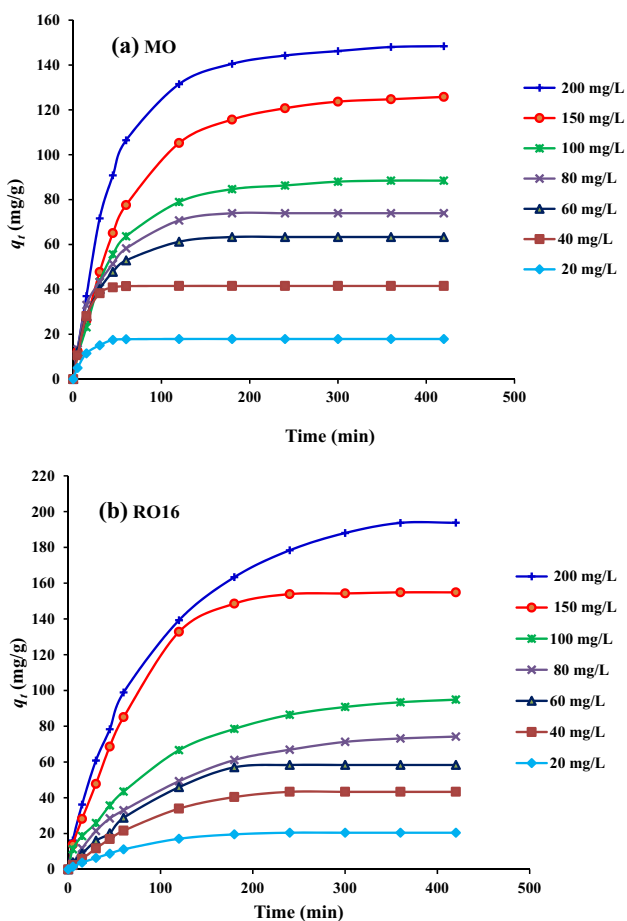


Fig. 8 Effect of the contact time on **a** MO and **b** RO16 adsorption at different initial concentrations (dosage 0.1 g, pH of solution 4, temperature 40 °C, agitation speed=90 strokes and volume of solution=100 ml)

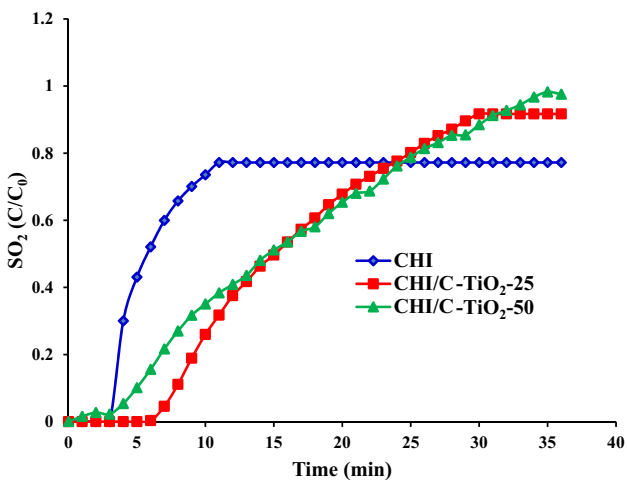


Fig. 9 Breakthrough curves of SO₂ capture over CHI, CHI/C–TiO₂-25, and CHI/C–TiO₂-50

Table 5 PFO and PSO kinetic parameters for the adsorption MO and RO16 on CHI/C–TiO₂-50

MO concentration (mg/L)	RO16 concentration (mg/L)	PFO		PSO	
		$q_{e, \text{exp}}$ (mg/gm)	k_1 (1/min)	$q_{e, \text{cal}}$ (mg/g)	$k_2 \times 10^{-2}$ (g/mg min)
20	20	17.9	0.066	19.1	0.565
40	40	41.5	0.072	44.3	0.261
60	60	63.3	0.034	68.5	0.072
80	80	73.9	0.030	80.5	0.053
100	100	88.5	0.021	99.6	0.026
150	150	125.8	0.016	147.0	0.012
200	200	148.4	0.021	167.1	0.015
20	20	20.4	0.013	25.8	0.507
40	40	43.3	0.011	56.7	0.186
60	60	58.4	0.011	77.1	0.134
80	80	74.2	0.009	94.8	0.099
100	100	94.9	0.010	119.1	0.085
150	150	154.8	0.013	193.0	0.070
200	200	193.7	0.011	239.1	0.048
					R^2
					0.94
					0.92
					0.99
					0.99
					0.99
					0.99
					0.99
					0.99
					0.98
					0.98
					0.97
					0.99
					0.99
					0.98
					0.99

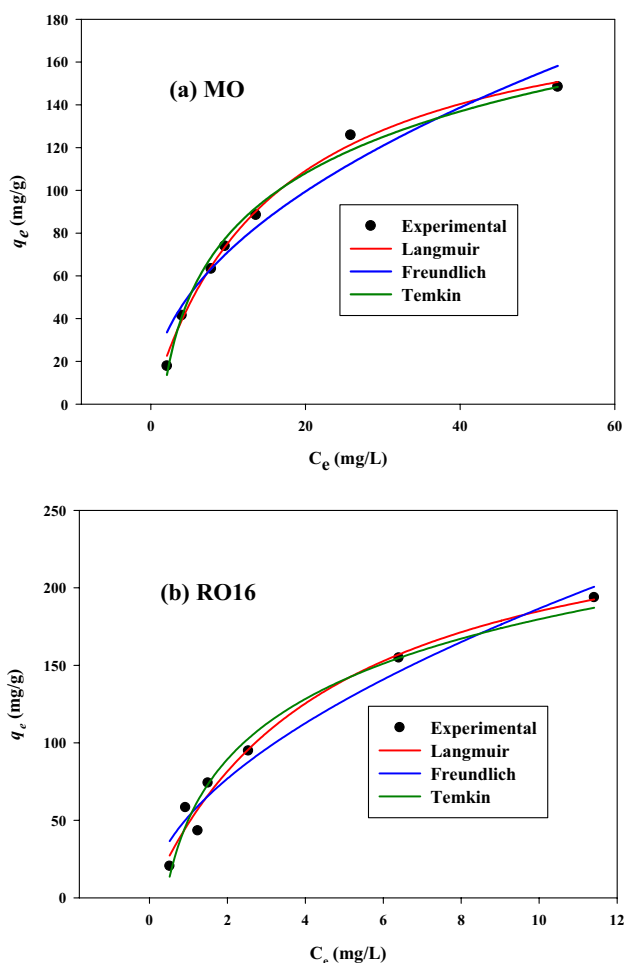


Fig. 10 Adsorption isotherms of **a** MO and **b** RO16 by CHI/C–TiO₂-50 (dosage 0.1 g, pH of solution 4, temperature 40 °C, agitation speed=90 strokes and volume of solution=100 ml)

Table 6 Parameters of the Langmuir, Freundlich and Temkin isotherm models for the adsorption of MO and RO16 on CHI/C–TiO₂-50 at 40 °C

Adsorption isotherm	Parameter	MO	RO16
Langmuir	q_m (mg/g)	196.6	270.5
	K_a (L/mg)	0.06	0.21
	R^2	0.99	0.98
Freundlich	K_f (mg/g) (L/mg) ^{1/n}	23.6	52.5
	n	2.08	1.81
	R^2	0.95	0.96
Temkin	K_T (L/mg)	0.406	0.89
	b_T (J/mol)	62.4	46.3
	R^2	0.98	0.97

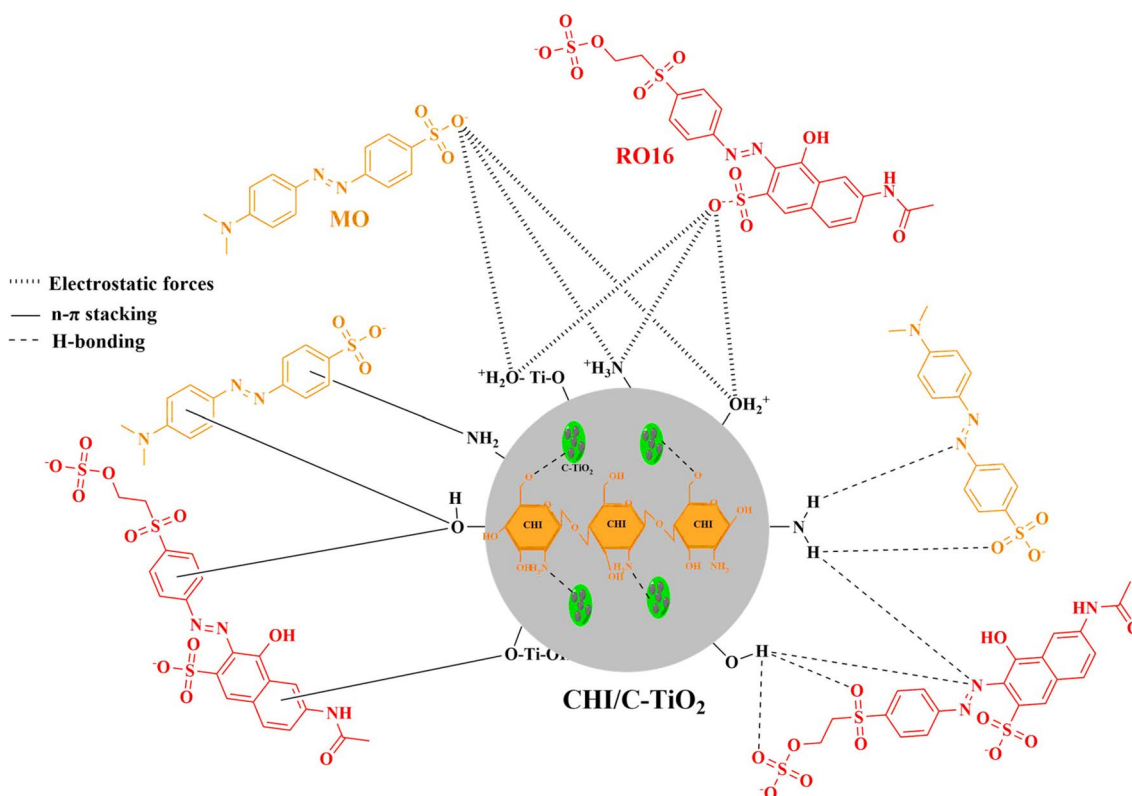
implicated in the adsorption of the MO and RO16 dyes via the interface that occurs between the CHI/C–TiO₂ surface (oxygen and nitrogen groups) and the aromatic rings of the MO and RO16 dyes [66].

Conclusion

A composite adsorbent with improved adsorption properties over pristine chitosan was reported herein. The composite is comprised of chitosan/C-doped TiO₂ (CHI/C–TiO₂) was found to be suitable for the removal of organic pollutants (methyl orange, MO; and reactive orange 16, RO16) and capture of an inorganic gas (SO₂). The best experimental conditions for the design of the composite adsorbent herein and the adsorption conditions for the highest removal of MO (81.6%) and RO16 (90.4%) dyes are as follows: C–TiO₂ loading = 50%, adsorbent dosage = 0.095 g, pH 4, and temperature = 40 °C. The results from the BBD model reveal that the highest MO and RO16 removal were obtained upon consideration of the following interactions: AB (C–TiO₂ loading × dose), AC (C–TiO₂ loading × pH), and BC (dose × pH). The results for the adsorption isotherms and the kinetic profiles showed that the adsorption process of MO and RO16 dyes onto the surface of CHI/C–TiO₂-50 is primarily monolayer adsorption and physisorption in nature. The maximum adsorption capacities of CHI/C–TiO₂-50 (containing 50% C–TiO₂) were found to be 196.6 mg/g and 270.5 mg/g of MO and RO16 dyes, respectively. The developed biocomposite material (CHI/C–TiO₂-50) was found to be an effective adsorbent for environmental applications such as the treatment of wastewater, along with gas capture, as shown for SO₂.

Table 7 Comparison of the adsorption capacity of CHI/C-TiO₂-50 toward the adsorption MO and RO16 dyes with various adsorbents

Adsorbents	Dye	q_{max} (mg/g)	Ref
CHI/C-TiO ₂ -50	MO	196.6	This study
CHI/C-TiO ₂ -50	RO16	270.5	This study
Crosslinked glyoxal-chitosan/TiO ₂ nanocomposite	MO	416.1	[38]
Chitosan coated sodium zeolite	MO	287	[54]
Bentonite modified with Ni-Fe layered double hydroxide	MO	215.9	[55]
Citrate-crosslinked Zn-MOF/chitosan	MO	202	[56]
Graphene oxide-MnO ₂ nanocomposite	MO	149.253	[57]
Chitosan-graphene oxide composite aerogel	MO	48.6	[58]
Chitosan biomass	MO	29	[59]
Residual brewery yeast	RO16	340	[60]
Ananas Comosus leaves activated carbon	RO16	147.05	[61]
Fly ash modified magnetic chitosan-polyvinyl alcohol blend	RO16	123.8	[62]
Magnetic crosslinked-chitosan/fly ash/Fe ₃ O ₄ biocomposite	RO16	112.5	[63]
Chitosan-fly ash/Fe ₃ O ₄	RO16	66.9	[64]
Magnetic clay/zeolitic imidazole framework nanocomposite	RO16	40.5	[65]

**Fig. 11** Illustration of the probable interaction between CHI/C-TiO₂ surface and MO and RO16 dyes including electrostatic forces, n- π stacking, and H-bonding

Acknowledgements The authors would like to acknowledge Faculty of Applied Sciences, Universiti Teknologi MARA, Shah Alam, for facilitating this research work. The authors would like to thank Universiti Teknologi MARA (UiTM) and Universitas Indonesia (UI) for supporting this research project by UiTM-UI Strategic Research Partnership

grants with grants numbers 100-RMC 5/3/SRP 052/2021 (UiTM) and NKB-674/UN2.RST/HKP.05.00/2021 (UI).

Author Contributions ASA: Formal analysis, Validation, Data Curation, Writing—Original; AHJ: Project administration, Formal analysis,

Validation, Data Curation, Writing—Original, Validation, funding acquisition, Project administration; MR: Project administration, Conceptualization, funding acquisition. TK: Validation, Data Curation. LDW: Writing—Review & Editing. ZMY: Formal analysis, Validation. All authors read and approved the final manuscript.

Funding This research project is funded by the Universiti Teknologi MARA (UiTM) and Universitas Indonesia (UI) under UiTM-UI Strategic Research Partnership grants with grants numbers 100-RMC 5/3/SRP 052/2021 (UiTM) and NKB-674/UN2.RST/HKP.05.00/2021 (UI).

Data Availability The datasets generated during and/or analysed during the current study are available from the corresponding author on reasonable request.

Declarations

Conflict of interest The authors have no relevant financial or non-financial interests to disclose.

References

- Ibrahim M, Labaki M, Giraudon JM, Lamonier JF (2020) Hydroxyapatite, a multifunctional material for air, water and soil pollution control: a review. *J Hazard Mater* 383:121139
- Abd-Malek NN, Yousif E, Jawad AH (2020) Optimization of adsorption parameters for reactive red 4 (RR4) removal by cross-linked chitosan-epichlorohydrin using Box Behnken design. *Sci Lett* 14(1):83–95
- Aigbe UO, Ukhurebor KE, Onyancha RB, Osibote OA, Darmokoesoemo H, Kusuma HS (2021) Fly ash-based adsorbent for adsorption of heavy metals and dyes from aqueous solution: a review. *J Mater Res Technol* 14:2751–2774
- Márquez AA, Sirés I, Brillas E, Nava JL (2020) Mineralization of Methyl Orange azo dye by processes based on H₂O₂ electrogeneration at a 3D-like air-diffusion cathode. *Chemosphere* 259:127466
- Wasim M, Sabir A, Khan RU (2021) Membranes with tunable graphene morphology prepared via Stöber method for high rejection of azo dyes. *J Environ Chem Eng* 9(5):106069
- Li X, Wang Z, Ning J, Gao M, Jiang W, Zhou Z, Li G (2018) Preparation and characterization of a novel polyethyleneimine cation-modified persimmon tannin bioadsorbent for anionic dye adsorption. *J Environ Manage* 217:305–314
- Braghiroli FL, Bouafif H, Koubaa A (2019) Enhanced SO₂ adsorption and desorption on chemically and physically activated biochar made from wood residues. *Ind Crops Prod* 138:111456
- Yang K, Yi H, Tang X, Zhao S, Gao F, Huang Y, Xie X (2019) Reducing the competitive adsorption between SO₂ and NO by Al₂O₃@TiO₂ core-shell structure adsorbent. *Chem Eng J* 364:420–427
- Abdulrasheed AA, Jalil AA, Triwahyono S, Zaini MAA, Gambo Y, Ibrahim M (2018) Surface modification of activated carbon for adsorption of SO₂ and NO_x: a review of existing and emerging technologies. *Rene Sustain Energy Rev* 94:1067–1085
- Xiao W, Jiang X, Liu X, Zhou W, Garba ZN, Lawan I, Yuan Z (2021) Adsorption of organic dyes from wastewater by metal-doped porous carbon materials. *J Clean Prod* 284:124773
- Guo D, Xiao Y, Li T, Zhou Q, Shen L, Li R, Lin H (2020) Fabrication of high-performance composite nanofiltration membranes for dye wastewater treatment: mussel-inspired layer-by-layer self-assembly. *J Colloid Inter Sci* 560:273–283
- Dewangan K, Singh D, Satpute N, Singh R, Jaiswal A, Shrivastava K, Bahadur I (2022) Hydrothermally grown α -MoO₃ microfibers for photocatalytic degradation of methylene blue dye. *J Mol Liq* 349:118202
- Chanikya P, Nidheesh PV, Babu DS, Gopinath A, Kumar MS (2020) Treatment of dyeing wastewater by combined sulfate radical based electrochemical advanced oxidation and electrocoagulation processes. *Sep Purif Technol* 254:117570
- Yagub MT, Sen TK, Afroze S, Ang HM (2014) Dye and its removal from aqueous solution by adsorption: a review. *Adv Colloid Inter Sci* 209:172–184
- Wong S, Ngadi N, Inuwa IM, Hassan O (2018) Recent advances in applications of activated carbon from biowaste for wastewater treatment: a short review. *J Clean Prod* 175:361–375
- Nor NM, Lau LC, Lee KT, Mohamed AR (2013) Synthesis of activated carbon from lignocellulosic biomass and its applications in air pollution control—a review. *J Environ Chem Eng* 1(4):658–666
- Pitchay T, Jawad AH, Johari IS, Sabar S (2022) Kinetics studies of metallic ions adsorption by immobilised chitosan. *Sci Lett* 16(1):137–148
- Abdalla TH, Nasr AS, Bassioni G, Harding DR, Kandile NG (2022) Fabrication of sustainable hydrogels-based chitosan Schiff base and their potential applications. *Arab J Chem* 15(1):103511
- Panda PK, Yang JM, Chang YH (2021) Preparation and characterization of ferulic acid-modified water soluble chitosan and poly (γ -glutamic acid) polyelectrolyte films through layer-by-layer assembly towards protein adsorption. *Int J Biol Macromol* 171:457–464
- Fan XD, Zhang XK (2013) Simultaneous removal of SO₂ and NO with activated carbon from sewage sludge modified by chitosan. *Appl Mech Mater* 253:960–964
- Ali HE, Nasef SM, Gad YH (2022) Remediation of Astrazon blue and Lerui acid brilliant blue dyes from waste solutions using amphoteric superparamagnetic nanocomposite hydrogels based on chitosan prepared by gamma rays. *Carbohydr Polym* 283:119149
- Jawad AH, Rangabhashiyam S, Abdulhameed AS, Syed-Hassan SSA, Alothman ZA, Wilson LD (2022) Process optimization and adsorptive mechanism for reactive blue 19 dye by magnetic crosslinked chitosan/MgO/Fe₃O₄ biocomposite. *J Polym Environ* 30(7):2759–2773
- Mohammadi E, Daraei H, Ghanbari R, Athar SD, Zandsalimi Y, Ziaee A, Yetilmezsoy K (2019) Synthesis of carboxylated chitosan modified with ferromagnetic nanoparticles for adsorptive removal of fluoride, nitrate, and phosphate anions from aqueous solutions. *J Mol Liq* 273:116–124
- Jawad AH, Abdulhameed AS, Selvasembian R, Alothman ZA, Wilson LD (2022) Magnetic biohybrid chitosan-ethylene glycol diglycidyl ether/magnesium oxide/Fe₃O₄ nanocomposite for textile dye removal: Box-Behnken design optimization and mechanism study. *J Polym Res* 29(5):1–15
- Vela N, Calín M, Yáñez-Gascón MJ, Garrido I, Pérez-Lucas G, Fenoll J, Navarro S (2018) Photocatalytic oxidation of six pesticides listed as endocrine disruptor chemicals from wastewater using two different TiO₂ samples at pilot plant scale under sunlight irradiation. *J Photochem Photobiol A Chem* 353:271–278
- Goldstein S, Behar D, Rabani J (2008) Mechanism of visible light photocatalytic oxidation of methanol in aerated aqueous suspensions of carbon-doped TiO₂. *J Phys Chem C* 112(39):15134–15139
- Shehzad H, Ahmed E, Sharif A, Farooqi ZH, Din MI, Begum R, Nawaz I (2022) Modified alginate-chitosan-TiO₂ composites for adsorptive removal of Ni (II) ions from aqueous medium. *Int J Boil Macromol* 194:117–127
- Cui HF, Wu WW, Li MM, Song X, Lv Y, Zhang TT (2018) A highly stable acetylcholinesterase biosensor based on

- chitosan-TiO₂-graphene nanocomposites for detection of organophosphate pesticides. *Biosens Bioelectron* 99:223–229
29. Qu L, Chen G, Dong S, Huo Y, Yin Z, Li S, Chen Y (2019) Improved mechanical and antimicrobial properties of zein/chitosan films by adding highly dispersed nano-TiO₂. *Ind Crops Prod* 130:450–458
 30. Rasoulzadeh H, Motesaddi Zarandi S, Massoudinejad M, Amini MM, Sheikhmohammadi A (2021) Investigation into the influencing factors and adsorption characteristics in the effective capture of carbon dioxide in flue gas by chitosan grafted Leca biocomposite. *Int J Environ Anal Chem*. <https://doi.org/10.1080/03067319.2021.2004408>
 31. Zhang W, Huang T, Ren Y, Wang Y, Yu R, Wang J, Tu Q (2021) Preparation of chitosan crosslinked with metal-organic framework (MOF-199)@ aminated graphene oxide aerogel for the adsorption of formaldehyde gas and methyl orange. *Int J Biol Macromol* 193:2243–2251
 32. Aboushouk MI, El-Zomrawy AA, Salem AM (2022) Electrochemical detection of H₂S gas based on chitosan extracted from shrimp shells loaded cadmium ions. *Egypt J Chem* 65(5):185–192
 33. Zhao J, Xi X, Ouyang H, Yang J, Wang Y, Yi L, Zhao L (2021) Acidic and alkaline gas sensitive and self-healing chitosan aerogel based on electrostatic interaction. *Carbohydr Polym* 272:118445
 34. Bayram A, Özbek C, Şenel M, Okur S (2017) CO gas sorption properties of ferrocene branched chitosan derivatives. *Sen Actuator B: Chem* 241:308–313
 35. Abdulhameed AS, Mohammad AT, Jawad AH (2019) Application of response surface methodology for enhanced synthesis of chitosan tripolyphosphate/TiO₂ nanocomposite and adsorption of reactive orange 16 dye. *J Clean Prod* 232:43–56
 36. Garg VK, Kumar R, Gupta R (2004) Removal of malachite green dye from aqueous solution by adsorption using agro-industry waste: a case study of *Prosopis cineraria*. *Dyes Pigm* 62(1):1–10
 37. Dalvand A, Nabizadeh R, Ganjali MR, Khoobi M, Nazmara S, Mahvi AH (2016) Modeling of reactive blue 19 azo dye removal from colored textile wastewater using L-arginine-functionalized Fe₃O₄ nanoparticles: Optimization, reusability, kinetic and equilibrium studies. *J Magn Mater* 404:179–189
 38. Mohammad AT, Abdulhameed AS, Jawad AH (2019) Box-Behnken design to optimize the synthesis of new crosslinked chitosan-glyoxal/TiO₂ nanocomposite: methyl orange adsorption and mechanism studies. *Int J Biol Macromol* 129:98–109
 39. Mostafa MH, Elsayy MA, Darwish MS, Hussein LI, Abdaleem AH (2020) Microwave-assisted preparation of Chitosan/ZnO nanocomposite and its application in dye removal. *Mater Chem Phys* 248:122914
 40. Noorimotlagh Z, Kazeminezhad I, Jaafarzadeh N, Ahmadi M, Ramezani Z, Martinez SS (2018) The visible-light photodegradation of nonylphenol in the presence of carbon-doped TiO₂ with rutile/anatase ratio coated on GAC: effect of parameters and degradation mechanism. *J Hazard Mater* 350:108–120
 41. dos Santos JM, Pereira CR, Pinto LAA, Frantz T, Lima ÉC, Foletto EL, Dotto GL (2019) Synthesis of a novel CoFe₂O₄/chitosan magnetic composite for fast adsorption of indigotine blue dye. *Carbohydr Polym* 217:6–14
 42. Melián EP, Díaz OG, Méndez AO, López CR, Suárez MN, Rodríguez JD, Peña JP (2013) Efficient and affordable hydrogen production by water photo-splitting using TiO₂-based photocatalysts. *Int J Hydro Energy* 38(5):2144–2155
 43. Jawad AH, Abdulhameed AS, Wilson LD, Hanafiah MAKM, Nawawi WI, Alothman ZA, Rizwan Khan M (2021) Fabrication of Schiff's base chitosan-glutaraldehyde/activated charcoal composite for cationic dye removal: optimization using response surface methodology. *J Polym Environ* 29(9):2855–2868
 44. Çathoğlu F, Akay S, Turunç E, Gözmen B, Anastopoulos I, Kayan B, Kalderis D (2021) Preparation and application of Fe-modified banana peel in the adsorption of methylene blue: process optimization using response surface methodology. *Environ Nanotechnol Monit Manage* 16:100517
 45. Jawad AH, Abdulhameed AS, Bahrudin NN, Hum NNMF, Surip SN, Syed-Hassan SSA, Sabar S (2021) Microporous activated carbon developed from KOH activated biomass waste: surface mechanistic study of methylene blue dye adsorption. *Water Sci Technol* 84(8):1858–1872
 46. Langhammer D, Kullgren J, Mitev P, Österlund L (2018) SO₂ adsorption on rutile TiO₂ (110): An infrared reflection-absorption spectroscopy and density functional theory study. *Surf Sci* 677:46–51
 47. Lagergren S (1898) Zur theorie der sogenannten adsorption geloster stoffe. *Vet Akad Handl* 24:1–39
 48. Ho YS, McKay G (1998) Sorption of dye from aqueous solution by peat. *Chem Eng J* 70:115–124
 49. de Souza APN, Licea YE, Colaço MV, Senra JD, Carvalho NM (2021) Green iron oxides/amino-functionalized MCM-41 composites as adsorbent for anionic azo dye: kinetic and isotherm studies. *J Environ Chem Eng* 9(2):105062
 50. Langmuir I (1918) The adsorption of gases on plane surfaces of glass, mica and platinum. *J Am Chem Soc* 40:1361–1403
 51. Frensdlich HMF (1906) Over the adsorption in solution. *J Phys Chem* 57:385–471
 52. Temkin MI (1940) Kinetics of ammonia synthesis on promoted iron catalysts. *Acta Physiochim URSS* 12:327–356
 53. Salem MA, Khan AM, Manea YK, Wani AA (2022) Nano chromium embedded in f-CNT supported CoBi-LDH nanocomposites for selective adsorption of Pb²⁺ and hazardous organic dyes. *Chemosphere* 289:133073
 54. Hussain S, Kamran M, Khan SA, Shaheen K, Shah Z, Suo H, Ghani U (2021) Adsorption, kinetics and thermodynamics studies of methyl orange dye sequestration through chitosan composites films. *Int J Boil Macromol* 168:383–394
 55. Sriram G, Bendre A, Altalhi T, Jung HY, Hegde G, Kurkuri M (2022) Surface engineering of silica based materials with Ni-Fe layered double hydroxide for the efficient removal of methyl orange: Isotherms, kinetics, mechanism and high selectivity studies. *Chemosphere* 287:131976
 56. Niu C, Zhang N, Hu C, Zhang C, Zhang H, Xing Y (2021) Preparation of a novel citric acid-crosslinked Zn-MOF/chitosan composite and application in adsorption of chromium (VI) and methyl orange from aqueous solution. *Carbohydr Polym* 258:117644
 57. Verma M, Tyagi I, Kumar V, Goel S, Vaya D, Kim H (2021) Fabrication of GO-MnO₂ nanocomposite using hydrothermal process for cationic and anionic dyes adsorption: kinetics, isotherm, and reusability. *J Environ Chem Eng* 9(5):106045
 58. Zhu W, Jiang X, Liu F, You F, Yao C (2020) Preparation of chitosan-graphene oxide composite aerogel by hydrothermal method and its adsorption property of methyl orange. *Polymer* 12(9):2169
 59. Allouche FN, Yassaa N, Lounici H (2015) Sorption of methyl orange from aqueous solution on chitosan biomass. *Proc Earth Planet Sci* 15:596–601
 60. Kim TY, Lee JW, Cho SY (2015) Application of residual brewery yeast for adsorption removal of Reactive Orange 16 from aqueous solution. *Adv Powder Technol* 26(1):267–274
 61. Ramachandran P, Vairamuthu R, Ponnusamy S (2011) Adsorption isotherms, kinetics, thermodynamics and desorption studies of reactive Orange 16 on activated carbon derived from *Ananas comosus* (L.) carbon. *J Eng Appl Sci* 6(11):15–26
 62. Abd Malek NN, Jawad AH, Ismail K, Razuan R, Alothman ZA (2021) Fly ash modified magnetic chitosan-polyvinyl alcohol blend for reactive orange 16 dye removal: adsorption parametric optimization. *Int J Boil Macromol* 189:464–476
 63. Abd Malek NN, Jawad AH, Abdulhameed AS, Ismail K, Hameed BH (2020) New magnetic Schiff's base-chitosan-glyoxal/fly ash/

- Fe₃O₄ biocomposite for the removal of anionic azo dye: an optimized process. *Int J Biol Macromol* 146:530–539
64. Jawad AH, Malek NNA, Abdulhameed AS, Razuan R (2020) Synthesis of magnetic chitosan-fly ash/Fe₃O₄ composite for adsorption of reactive orange 16 dye: optimization by Box–Behnken design. *J Polym Environ* 28(3):1068–1082
65. Ecer Ü, Zengin A, Şahan T (2021) Magnetic clay\zeolitic imidazole framework nanocomposite (ZIF-8@ Fe₃O₄@ BNT) for reactive orange 16 removal from liquid media. *Colloids Surf A* 630:127558
66. Singh SK, Das A (2015) The n → π* interaction: a rapidly emerging non-covalent interaction. *Phys Chem Chem Phys* 17(15):9596–9612

Publisher's Note Springer Nature remains neutral with regard to jurisdictional claims in published maps and institutional affiliations.